ACS OMEGA

Open Access

http://pubs.acs.org/journal/acsodf

Article

Molding Quality and Biological Evaluation of a Two-Stage Titanium Alloy Dental Implant Based on Combined 3D Printing and Subtracting Manufacturing

Hongbo Wei,[†] Shitou Huang,[†] Yi Liu, and Dehua Li*

Cite This: *ACS Omega* 2024, 9, 51591−51603

Read Online

ACCESS | Metrics & More | Article Recommendations

ABSTRACT: Metal 3D printing has been used in the manufacturing of dental implants. Its technical advantages include high material utilization and the capacity to form arbitrarily complex structures. However, 3D printing alone is insufficient for manufacturing two-stage titanium implants due to the limited precision in printing titanium alloy parts. In this study, 3D printing was employed to create the implant structure, subsequently complemented by mechanical processing to refine the implant abutment connection and neck. Additionally, the mechanical properties of 3D-printed titanium alloy implants were evaluated through tensile and dynamic fatigue testing. The MTT assay was employed to assess the cytotoxicity of 3D-printed titanium alloy dental implants. The impact of bone union and osteogenesis from 3D-printed titanium alloy dental implants was investigated through in vivo experimentation. The results demonstrated that combining 3D printing with subsequent machining constitutes a viable method for the manufacture of two-stage titanium dental implants. Test results for mechanical properties indicated that heat-treated 3D-printed titanium alloy dental implants possess significant tensile strength and fatigue resistance and are capable of withstanding the robust chewing forces in the oral cavity. In vitro findings revealed that sandblasted and acid-etched 3D-printed titanium alloy exhibited negligible cytotoxicity, with osteoblast differentiation of hMSCs being more pronounced compared with the control group. In vivo studies indicated that no significant differences were observed in bone volume fraction, bone−implant contact rate, and unscrewing torque between 3D-printed titanium alloy dental implants and commercial SLA surface implants at both 1 and 3 months postimplantation.

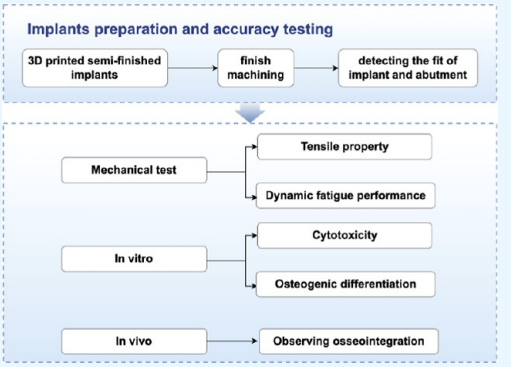

1. INTRODUCTION

The global demand for dental implants has experienced a substantial and sustained increase, reflecting an increasing recognition of their critical role in dental restoration. Specifically, in China, the utilization of dental implants increased from 1.96 million in 2017 to 4.18 million by 2021, indicating a significant annual growth of 15.47% from the previous year.[1] Dental implants, which consist of the implant itself, abutments, and crowns, are fundamental to a successful denture restoration. The implant, acting as an artificial root, is surgically embedded into the maxilla or mandible to secure the denture's superstructure. Titanium and its alloys are predominantly the materials of choice for these implants, owing to their biocompatibility and mechanical properties.[2] Implant dentures consist of implants, abutments, and crowns with the implant being regarded as the most critical component. The production mode of a titanium implant is usually formed by subtracting manufacturing (SM) from a titanium bar.[3] However, the cutting process results in material waste. Additionally, the significant mismatch between the elastic modulus of dense titanium and jawbone tissue may lead to a "stress shielding effect," which has become a growing concern in oral implantology.[4]

Additive manufacturing (AM) represents a potential approach to addressing these issues. AM operates on the discrete stacking principle, utilizing three-dimensional data to fabricate parts directly. This process thereby reduces material waste and is theoretically capable of producing parts with arbitrarily complex shapes.[5,6] Furthermore, drawing on the bionic design concept, some scholars employ AM to fabricate root analogue implants (RAI).[7] A RAI represents a type of implant designed to match the shape of a missing tooth. Importantly, its design obviates the need for predrilling, thereby reducing damage to surrounding bone and soft tissue.[8] However, despite these advances, the lack of a unified standard

Received: October 7, 2024
Revised: November 16, 2024
Accepted: December 12, 2024
Published: December 19, 2024

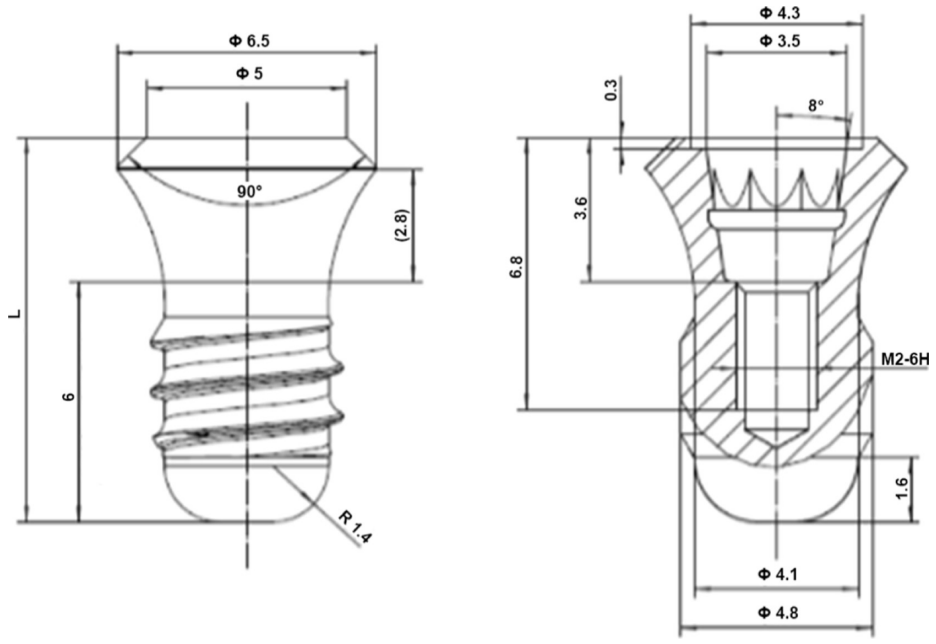

Figure 1. Two-dimensional parts of the implant.

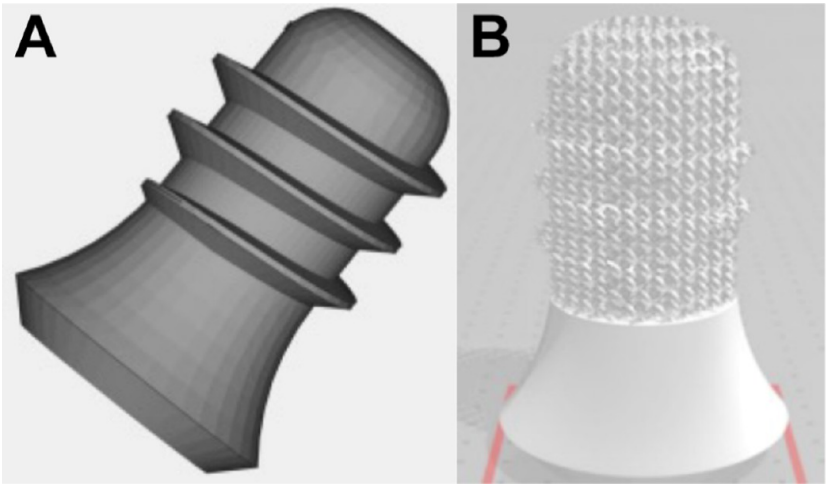

Figure 2. (A) 3D model of the implant and design of the (B) porous structure on the implant surface.

for the manufacturing materials, methods, and morphological design of RAI has limited its clinical application.[9]

Additionally, the two-stage implant is most commonly used in clinical settings.[10] The implant and abutment of two-stage implants are separate components, allowing for either submerged or nonsubmerged placement. Moreover, the connection structure within the abutment of the two-stage titanium implant must be highly smooth and ensure a tight fit with the abutment.[3] Unfortunately, achieving direct and high-precision forming of parts, especially those requiring assembly, is challenging due to AM's significant limitations in controlling forming accuracy and surface quality. Consequently, using AM to manufacture two-stage implants with abutment connection structures proves challenging.[11,12]

A potential solution involves combining AM with SM. SM, which is based on the material "removal" principle, demonstrates excellent performance in forming accuracy and surface quality control.[13] Therefore, this study aims to report on a combined AM/SM manufacturing flow for a two-stage implant. Furthermore, this study evaluates the important mechanical properties and conducts biological evaluations both in vitro and in vivo.

2. MATERIALS AND METHODS

2.1. Shape and Structure Design of a Two-Stage Titanium Implant. The outline and structure design of the two-stage titanium implant refer to the outline and structure design of the classical soft tissue horizontal implant. First, the implant parts were drawn using AutoCAD software (Figure 1). The length of the internal bone segment was 6 mm. The diameter was 4.8 mm. The thread parameters were M2-6H. The maximum outer diameter of the gingival segment was 6.5 mm and the height was 2.8 mm. The two-dimensional diagram shows the final shape and structure design of the implant. The dimensional marks in the diagram clearly show the shape and structure of the implant and their mutual positions and contain the technical requirements such as dimensional accuracy. In addition, a titanium sheet of 15 × 1.5 mm and an implant of

https://doi.org/10.1021/acsomega.4c09131
ACS Omega 2024, 9, 51591−51603

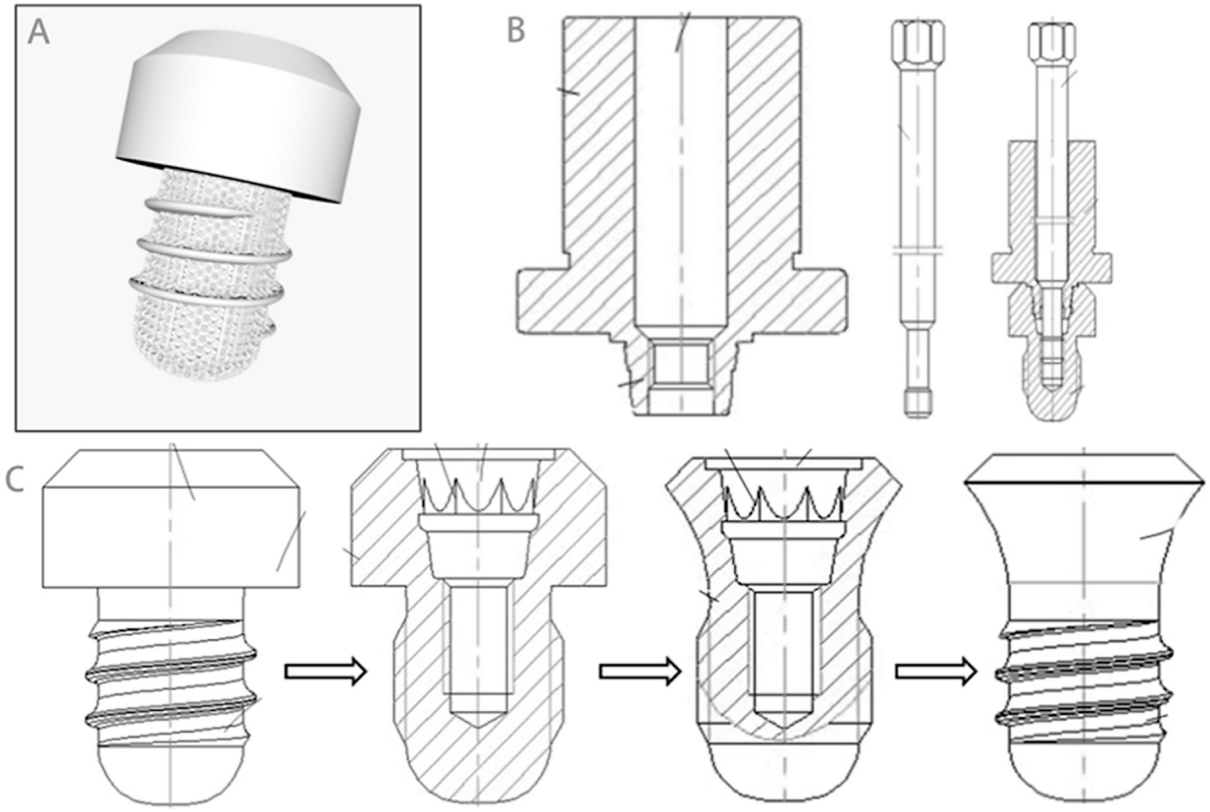

Figure 3. (A) 3D structure model of the 3D-printing implant. (B) Fixture used in processing implants. (C) Reduction process of the 3D-printing titanium implant.

3.3 × 8 mm were also designed for in vitro cell experiment and in vivo experiment.

In SolidWorks software, a 3D model of the implant is constructed, as shown in Figure 2A. The porous structure of the implant surface was designed: 150 μm thickness, 300 μm aperture, 100 μm edge diameter, diamond structure (Figure 2B). At the same time, the modeling software was used to establish the standard cube test block for the molding accuracy test: 10 mm × 10 mm × 10 mm, and the tensile specimen: The original distance length is 55 mm. The parallel length is 75 mm. The width is 10 mm. The thickness is 2 mm.

2.2. Materials and Samples Preparation. The base material is Ti-6Al-4 V powder prepared by plasma wire atomization (Chengdu optimal material Co., Ltd., China) with a particle size of 14.22 μm−88.91 μm. All the samples evaluated in this study were manufactured by an SLM machine (iSLM500QN, ZRapidTech, Jiangsu, China) at a scanning speed of 4.0 m/s, a laser power of 500 W, a spot size of 0.20 mm, and a layer thickness of 0.05 mm. The forming process was carried out in a processing chamber filled with argon. After production, the samples were removed from the substrate using wire electro-discharge machining. The model diagram of a 3D-printed semifinished implant is shown as Figure 3A. The heat treatment of the obtained samples was as follows: in a 99.99% argon environment, the temperature is heated to 820 °C for 1.5 h and then cooled to 200 °C with a furnace. The samples were ultrasonically cleaned with acetone, ethanol, and distilled water and then dried at room temperature for follow-up treatment.[14]

A fixture (Figure 3B) for fixing the implant during subsequent machining was designed according to the shape of the semifinished implant. The mechanical shaping of the abutment connection structure and the neck of the SLM titanium implant was performed by Trausim Co., Ltd. (China). The implant-related components, such as the abutment used in this study, were also provided by Trausim company. Therefore, the shape and internal thread parameters (tooth shape, diameter, number of lines, pitch and guide, and rotation direction) of the implant abutment were consistent with the finished abutment provided by the company. The specific method for subsequent subtractive manufacturing of 3D-printed titanium implants is shown in Figure 3. The implant semifinished product was first prepared using AM technology. The body of the implant remains unchanged and is regarded as the body. Only the gingival perforating segment is processed twice, while the cylindrical perforating segment can be regarded as the embryo. In the next step, the side wall of the embryo body is clamped, and the top of the embryo body is treated by machining equipment to form the abutment connecting cavity. After the inner cavity is processed, the next step is to connect the fixed device. The lower end of the fixed device is matched with the base platform connecting cavity, and the fixed device is installed on the connecting cavity and then fixed with the connecting bolt, so as to lock the mutual position of the semifinished implant and the fixed device. Finally, the processing equipment is used to remove the excess part of the fetal body by holding the fixed device. The final neck shape of the implant is formed. At this point, the final product of the implant is processed.

After the final processing of the implant, we carried out sandblasting and acid-etching treatment. It is divided into four steps: cleaning and removing oil: the implant goes through ultrasonic cleaning with degreasing solution, rinsing with tap water, ultrasonic cleaning with purified water, and drying;

https://doi.org/10.1021/acsomega.4c09131
ACS Omega 2024, 9, 51591−51603

sandblasting treatment: white corundum is used to sandblast the surface of the titanium implant. Acid etching treatment: The acid-etching solution consists of concentrated sulfuric acid, concentrated hydrochloric acid, and deionized water according to a certain volume ratio; the final cleaning: the dental implants after acid etching are successively passed through purified water spray—purified water ultrasonic cleaning—purified water irrigation—purified water ultrasonic cleaning—drying.[15]

2.3. Compatibility between the Implant and Abutment. The implant and its matching abutment are assembled and fixed according to the instructions provided by the manufacturer. The assembled implant and abutment were embedded into dental self-setting resin. After the self-curing resin was completely cured, it was cut into two halves along the long axis of the implant. Half of the cutting surfaces are polished. We used a metallography microscope (MN80, Trulli Material Technology Co., Ltd., China) to observe the fit gap (including vertical fit gap and conical fit gap, i.e., the maximum vertical distance from the end to the opposite side) between the implant and the abutment. The magnification was 500 times, and the distance between the eyes was 50 mm. The gap was measured using the ImageView view control. A total of 5 samples were measured.

2.4. Measurement of Forming Accuracy and Surface Roughness. The dimensional accuracy of the SLM titanium alloy cube was measured by a micrometer and measured from three directions of *X*, *Y*, and *Z* axes. The number of test samples was 5. The micrometer used in this test is a high-precision measuring tool. Preparation tool: digital micrometer (Mitutoyo, Japan): Specification 0−25 mm, resolution: 0.001 mm. The calibration was checked to ensure it is accurate. Cube sample: It was ensured that the surface of the cube sample is clean and free of damage. Sides measurement: A micrometer was used to measure each of the three sides of the cube (length, width, and height). Several different positions on each side were chosen to measure, and the average was taken to reduce error. The data of each measurement and for subsequent calculation and analysis was recorded.

Additionally, the roughness of the controlled and experimental implants was measured by using a 3D optical profilometer (Contour GT-K 3D, Bruker, MA, USA). Three specimens from each group were measured with vertical scanning interferometry with a 1× magnification lens, a field of view of 0.4 × 0.4 mm, and a scan speed of ×1. The "VXI" mode was used to reduce the noise level in the flat area. Furthermore, the tested areas were reconstructed in 3D to visualize the surface topographies.

2.5. Mechanical Properties Measurement. According to the GB/T228-2010 tensile test of metal materials, we prepared a 3D-printed tensile test rod after machining. The tensile test rod before and after heat treatment was placed on the electronic hydraulic universal material testing machine (Instron5985, maximum load 50 kN × 2.5 kHz sampling rate, Boston, Massachusetts, USA). Its tensile properties were tested (tensile strength (Rm), specified nonproportional extension strength (Rp), elongation after fracture (*A*), and section shrinkage (*Z*)). The calculation method is based on GB/T228-2010. When the surface is stretched, displacement control is used. The loading speed is 1 mm/min. The fracture morphology of the tensile specimen was observed by 5000× magnification of a scanning electron microscope. The fracture form was analyzed. Before observation, the sample was cleaned with alcohol solution in an ultrasonic cleaner for about 5 min[16]

The dynamic fatigue test device of the implant is shown in Figure 4. According to the test requirements, the clamping

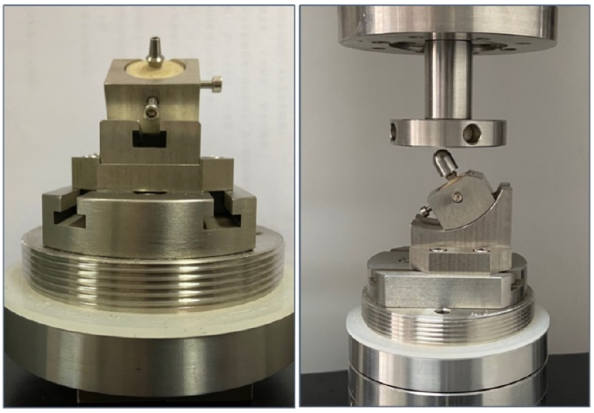

Figure 4. Dynamic fatigue testing device was used to determine the dynamic mechanical stability of the 3D-printing implant.

position of the fixed block should be placed at the root square 3 mm ± 0.5 mm at the junction of the rough implant and the smooth collar. After fixing the implant, the abutment was installed and a torque meter was used to tighten the abutment screw (30 N cm). Test environment: carried out in the air at a temperature of 20 ± 10 °C; loaded with a positive spin wave, with an angle of 30° with the axis of the implant, load F = 200 N, 5 × 10^6 cycles, frequency 15 HZ. A total of 3 samples were tested.

Additionally, the density of the implants was measured. An object immersed in a liquid experiences an upward buoyant force equal to the weight of the liquid displaced by the object. Using an electronic balance, the weights of the solid in air and in the liquid are measured as Wa and W^f1, respectively. Neglecting the buoyant force of the air, and given that the density of the liquid is $\rho f1$, the density of the implant can be calculated according to the following formulation[17]

$$\rho = \frac{\mathrm{Wa}\cdot\rho f1}{\mathrm{Wa} - W^f1}$$

2.6. In Vitro Experiments. *2.6.1. MTT Assay.* The weight of the implant sample was weighed, and the 0.2 g/mL extraction ratio was added to the cell culture medium at 37 °C. The extract was prepared 24 h later. Osteoblasts cultured for 48 h were inoculated in a 96-well plate with 1 × 10^4 cells/mL suspension. Each group had 5 holes at each time point. After 24 h of culture, the culture medium was discarded. The extract was added in the experimental group, and the cell culture medium was added in the control group. MTT was added at the time points of 1, 3, and 5 days and cultured for 4 h. The absorbance was determined at 490 nm of the enzyme labeling instrument. The experiment was divided into two groups: group A was the SLM titanium sheet extract group, and group B was the blank control group with 3 titanium slices in each group.

2.6.2. Alizarin Red Staining. The single cell suspension of 2 × 10^4 BMSC was applied to the SLM titanium discs and the 12-well plate (control group). After osteogenic induction for 14 days, Alizarin red staining was performed to assess the mineralization level on the SLM titanium discs. Samples were

https://doi.org/10.1021/acsomega.4c09131
ACS Omega 2024, 9, 51591−51603

washed in phosphate buffered saline (PBS) and then fixed in 4% paraformaldehyde for 30 min. After being washed two times in PBS, samples were stained in Alizarin red staining solution (Cyagen Biosciences, China) and then washed in distilled water thoroughly and dried in air. Samples were observed under a stereomicroscope (Leica M205FA, Germany), and images were obtained by a charge-coupled device sensor and camera system. To quantify the mineralization, each sample was emerged in 1 mL of 10% hexadecylpyridinium chloride (Sinopharm Chemical Reagent Co., Ltd.) for 10 min at 37°. Then 100 μL of solution from each well was transferred into a 96 well to detect the absorbance at 562 nm.

2.7. In Vivo Experiments. *2.7.1. Surgical Procedure.* Studies involving animals were approved by the Tab of Laboratory Animal Ethical Inspection, School of Stomatology, Air Force Military Medical University (approval code: 2021053), and all treatments to the animals were performed in accord with ARRIVE guidelines. A total of three beagles were used in the experiment. Adult male beagle dogs were anaesthetized by injecting xylazine hydrochloride (0.1 mL/kg) and 2.5% pentobarbital sodium solution (0.5 mL/kg) into the gluteus maximus muscle. Oral disinfection was performed with 1% iodophor, and local infiltration anesthesia was performed in bilateral mandibular premolars with articaine hydrochloride injection. The teeth were divided into proximal and distal parts with a carborundum needle. The roots were stiffened and loosened, and the second, third, and fourth premolars were extracted sequentially.

Three months after the healing of the tooth extraction wound, the three sites on each side of the mandible of each beagle were divided into the left/right proximal, middle, and distal parts. One side was randomly selected as the experimental group and the other as the control group. Two implants were implanted in each side first, among which the distal part was the spin-out experimental group; the other one was randomly selected in the mesial or middle position, and the control group was implanted in the opposite side in the same position. After another 2 months, experimental implants were implanted on one side of the experimental group and on the other side of the control group. Another month later, after the animals were killed, implant samples with bone chunks were removed for follow-up experiments. Experimental group: SLM implant; control group: SLA surface implant; product specifications: rough surface, length 8 mm, diameter 3.3 mm, through the gingival height 2.8 mm.

2.7.2. Micro-CT Scanning. After 4 and 12 weeks of recovery, bone formation in the beagle model was evaluated by using a micro-CT scanner at a scan resolution of 12 mm. 3D images were constructed and analyzed with 3D modeling software (VG Studio Max, Volume Graphics, Heidelberg, Germany). Bone volume/total volume (Bv/Tv) was calculated using 0.2 mm around the implant as the target area.

2.7.3. Histomorphological Analyses. 2.7.3.1. Specimens Preparation. Four and twelve weeks after implantation, the implants were entirely removed from the rats followed by 48 h formalin fixation, decalcification, and insertion into resin. Ground sections of 300 μm thickness were made using high-precision diamond disc slicing (Leica SP 1600, Leica, Wetzlar, Germany). Decalcified sections of approximately 70 μm thickness were then made by using a grinder (RotoPol-35, Struers, FL, USA). The specimens were stained by Van Gieson (VG) using the standard method.

2.7.3.2. Specimens Observation. A stereoscopic microscope (DMI6000B, Leica Microsystems, Shanghai, China) was used to observe the prepared specimens to analyze the morphologic features of the bone tissue around the implant and the interface of the implant. Images were taken at 20× magnification and analyzed by an imaging system (Leica Imaging System, Cambridge, UK). The bone−implant contact rate (BIC %) was obtained by calculating the ratio of the entire length of the implant to the BIC area using ImageJ software.

2.7.4. Removal Torque Measurements. Four and twelve weeks after recovery, the beagle dogs were sacrificed, and the soft tissues were elevated to expose the implantation sites. The implant was fixed with a removal tool that was connected to a digital torque gauge (MGT-12, Mark-10, Copiague, NY, USA). As the torque gradually increased, the critical torque value to destroy the implant−tissue adherence was recorded as the maximum removal torque.

3. RESULTS

3.1. Measurement of Forming Accuracy. The two-stage implant was successfully manufactured by using AM/SM technology (Figure 5). Figure 6 displays an scanning electron microscopy (SEM) image depicting the surface of the SLM titanium alloy implant at a magnification of 30 times. The image reveals a porous structure with pore diameters approximately 300 μm, evenly distributed across the implant's surface. Notably, the implant exhibits no apparent surface defects, such as cracks, and features a naturally rough appearance.

Figure 5. Representative images of the 3D-printing titanium implant. (A) Printed implant (neck-processed). (B) The implant is connected with the carrier and the (C) repair abutment.

The test result of forming accuracy shows that the dimensional accuracy of each test sample is within the tolerance range (<0.08 mm), as shown in Table 1.

3.2. Fit Gap between the Implant and Abutment. The implant was bisected along its long axis. Subsequently, half of the bisected surfaces were polished, and the fit gap between the implant and the abutment was quantified using an optical

https://doi.org/10.1021/acsomega.4c09131
ACS Omega 2024, 9, 51591−51603

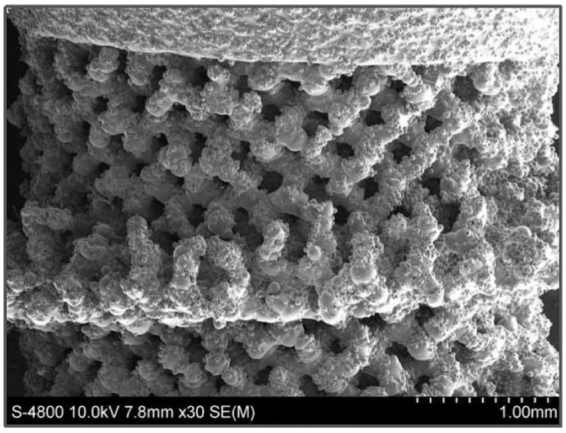

Figure 6. SEM images of the surface of the SLM implant.

Table 1. Printing Accuracy of the Implant

number	axial	nominal value (mm)	common difference (mm)	actual measured value (mm)
#1	*X*	10.00	±0.08	10.00
	Y	10.00	±0.08	10.01
	Z	10.00	±0.08	10.03
#2	*X*	10.00	±0.08	10.01
	Y	10.00	±0.08	10.01
	Z	10.00	±0.08	10.02
#3	*X*	10.00	±0.08	9.99
	Y	10.00	±0.08	10.01
	Z	10.00	±0.08	10.01
#4	*X*	10.00	±0.08	10.01
	Y	10.00	±0.08	10.01
	Z	10.00	±0.08	10.01
#5	*X*	10.00	±0.08	10.00
	Y	10.00	±0.08	9.99
	Z	10.00	±0.08	10.01

measuring instrument (Figure 7). The measured maximum gap amounted to merely 6.36 μm.

3.3. Surface Characterizations and Roughness. Figure 8 depicts the SEM images before and after sandblasting and acid etching. At a magnification of 3000 times, one can observe unmelted and loose powder particles with a particle size of 25−30 μm on the implant's surface prior to sandblasting and acid etching. Following sandblasting and acid etching, there was a significant reduction in loosely bound particles, accompanied by the emergence of numerous micron/nanometer-scale pit-like structures. Compared to the control group, the surface of the implants in the experimental group was rougher and exhibited greater variations in topography. The surface of the control group ranged from −17.9 to 9.2 μm, while the −27.7 to 28.3 μm (Figure 8C). Quantitative analysis of surface roughness by Ra and Rq values also shows that the surface roughness of the experimental implant has a rougher surface compared to the control group (Figure 8D,E).

3.4. Mechanical Properties. Through the tensile test, the tensile properties such as tensile strength, yield strength, elongation, and fracture surface shrinkage are obtained (Table 2). From the macroscopic morphology of the fracture surface of the tensile sample (Figure 9A), it can be seen that the fracture surface of the annealed SLM titanium alloy appears to be necking. Figure 7B,C displays pronounced dimples within the sample's cross section, characterized by their larger and deeper appearance. Concurrently, the findings of the tensile test on the improvement in fracture elongation rate corroborate the microstructural observations. However, the macroscopic fracture surface of the SLM titanium alloy, without heat treatment, shows no evident necking. Electron microscopy revealed the typical characteristics of an intergranular brittle fracture, indicating poor plasticity. Dynamic fatigue performance testing results indicated that, under prescribed conditions, the implant sustained no damage after 5 million impacts (Figure 10). Further, the density of the implants was measured with an average density of 4.08 g/cm^3.

3.5. In Vitro Studies. *3.5.1. MTT Assay.* The results indicated that the SLM titanium alloy exhibited no cytotoxicity. Following coculture with cells, the optical density (OD) values for both the experimental and control groups demonstrated an increasing trend over time. Figure 11 illustrates that no significant differences were observed in OD values between the two groups on the first, third, and fifth days postinoculation, suggesting that SLM titanium plates did not significantly affect MG-63 cell proliferation. On the first, third, and fifth days, the relative growth rates of the experimental and control groups were 100%, 93%, and 97%, respectively. According to the grade 5 toxicity standards, the cytotoxicity level was classified as grade 0.

3.5.2. Osteogenic Differentiation. Figure 12 depicts the deposition of the mineralized matrix on the 14th day. As illustrated in Figure 8, BMSCs demonstrate effective cell differentiation in both experimental and control groups. The

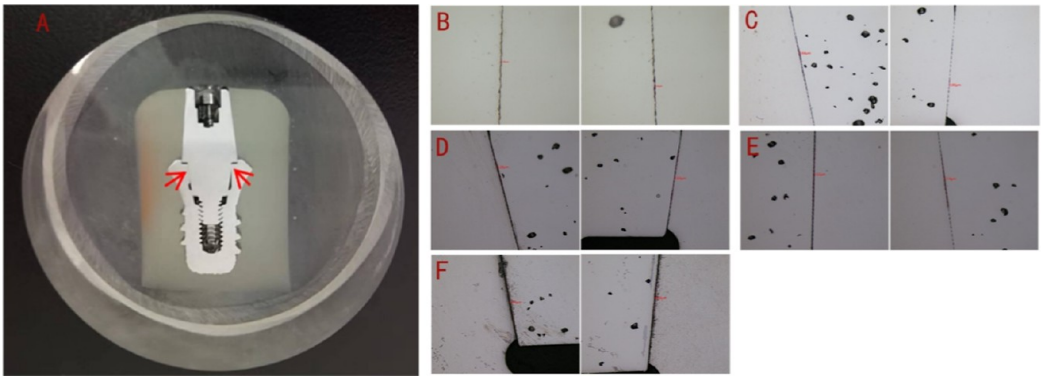

Figure 7. Images showing the fit gap between the implant and abutment. (A) Clearance fit sample profile. (B−F) the fit gaps of 5 samples were measured.

https://doi.org/10.1021/acsomega.4c09131
ACS Omega 2024, 9, 51591−51603

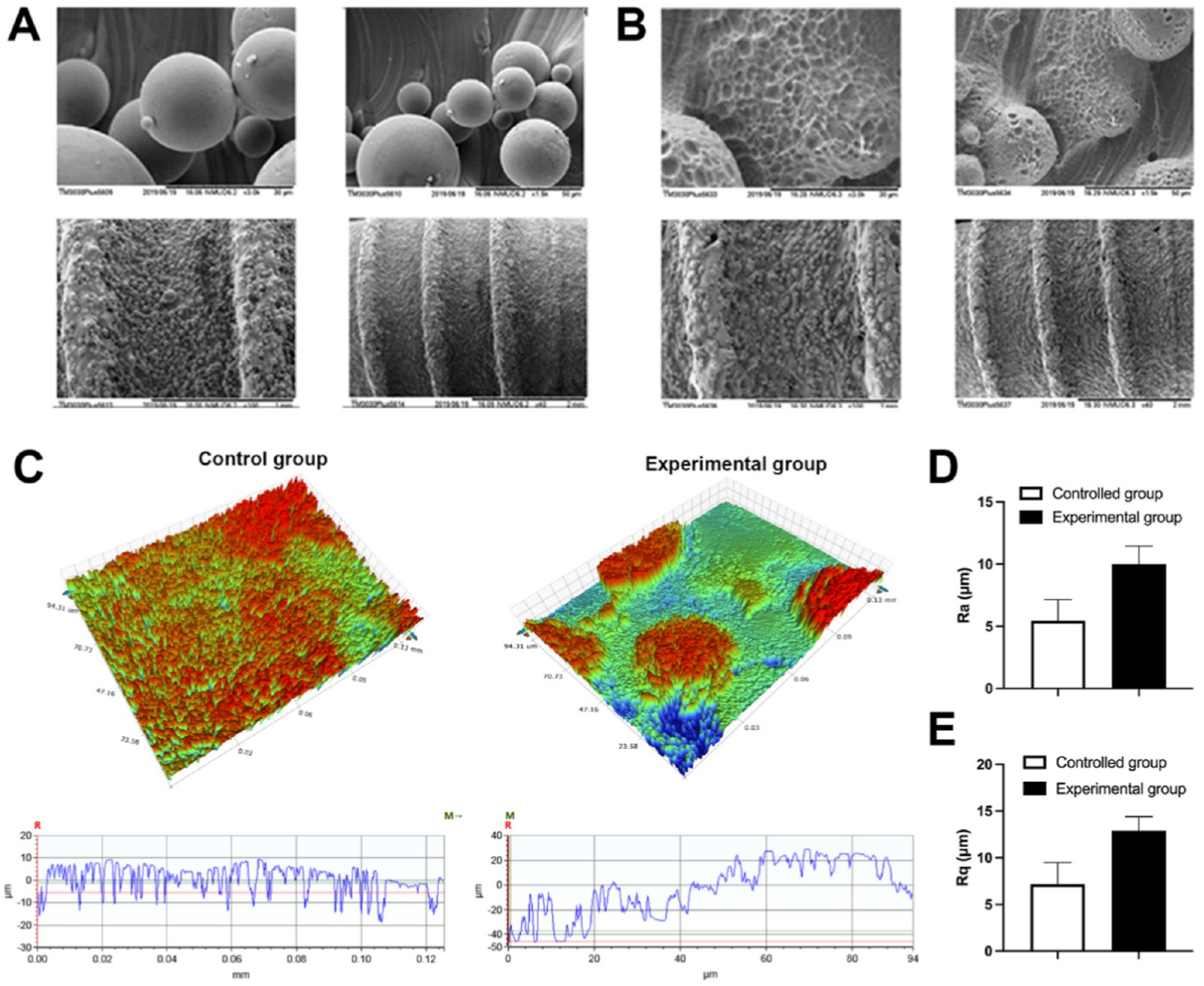

Figure 8. SEM images of the implant surface (A) before and (B) after sandblasting and acid etching. (C) Reconstructed three-dimensional images of control and experimental implants surfaces and roughness analysis. Quantitative analysis of surface roughness of control and experimental implant surfaces by the (D) Ra value and (E) Rq value (n = 5). Data are presented as mean ± SD.

Table 2. Mechanical Properties of Three-Dimensional-Printed Titanium Alloy Specimens

number	R_m/Mpa	$R_{p0.2}$/Mpa	A %	Z %
#1	978	918	17	43
#2	975	917	15	25
#3	971	914	16	29

results indicate that SLM titanium plates facilitate osteogenic differentiation of BMSCs.

3.6. In Vivo Studies. *3.6.1. Micro-CT Scanning.* The 3D-reconstructed micro-CT images of SLM implants and control implants are shown in Figure 13. In these images, the implant and cancellous bone are marked in white and yellow, respectively. The bone volume surrounding the SLM implant is comparable to that surrounding the SLA surface implant.

3.7. Histomorphological Analyses. Figure 14A,B presents the histological images and BIC percentage results. Following 1 and 3 months of recovery, robust bone integration was observed on the implant surfaces in both the experimental and control groups. The BIC values between the two groups exhibited no significant differences.

3.8. Removal Torque Measurements. Figure 15 summarizes the removal torque values for both groups at 4 and 12 weeks. Following 4 and 12 weeks of recovery, the removal torque between the SLM and SLA groups showed no significant differences.

4. DISCUSSION

As a technology capable of producing customized metal products, emerging AM technology is considered to possess significant application potential in dental implants. However, before employing AM titanium implants in clinical practice, the challenge of processing the implant's connecting structure must be addressed.[18] In this study, a composite manufacturing approach combining additive and subtractive methods was utilized to address this issue. The initial near-net shaping of the implant was conducted by using AM technology, followed by finishing through traditional machining. The fit gap between the implant and the abutment was measured, revealing a maximum gap of only 6.36 μm and confirming excellent

https://doi.org/10.1021/acsomega.4c09131
ACS Omega 2024, 9, 51591−51603

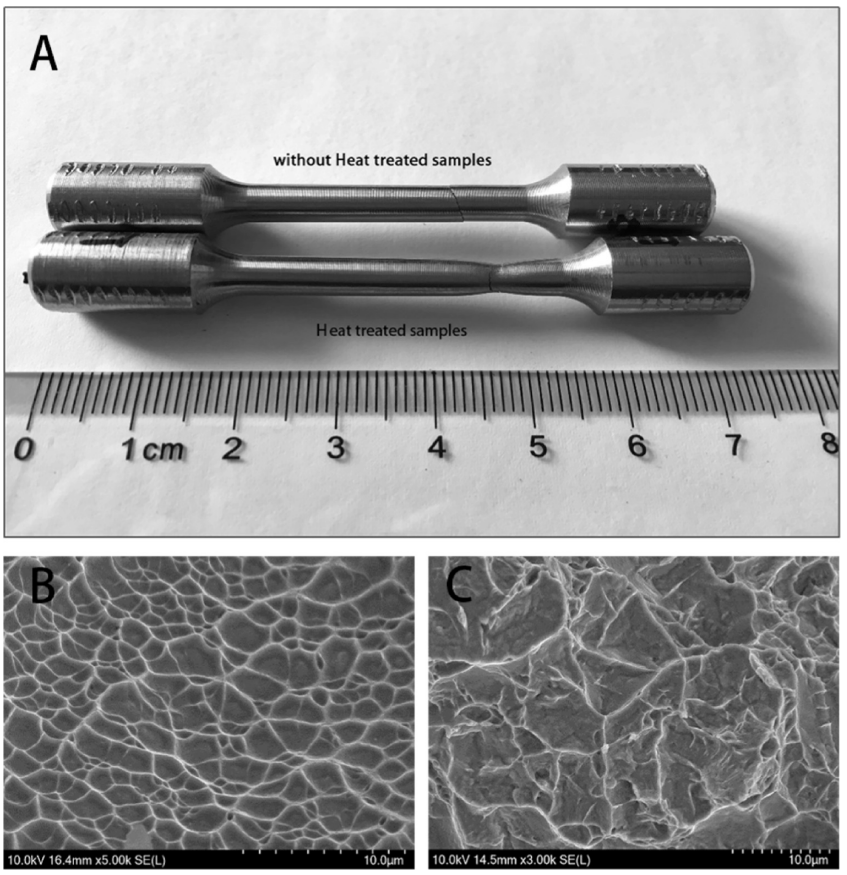

Figure 9. Photographs and SEM images of samples before and after heat treatment. (A) Physical image of the tensile specimen. SEM image of the sample fracture surface. (B) Before heat treatment. (C) After heat treatment.

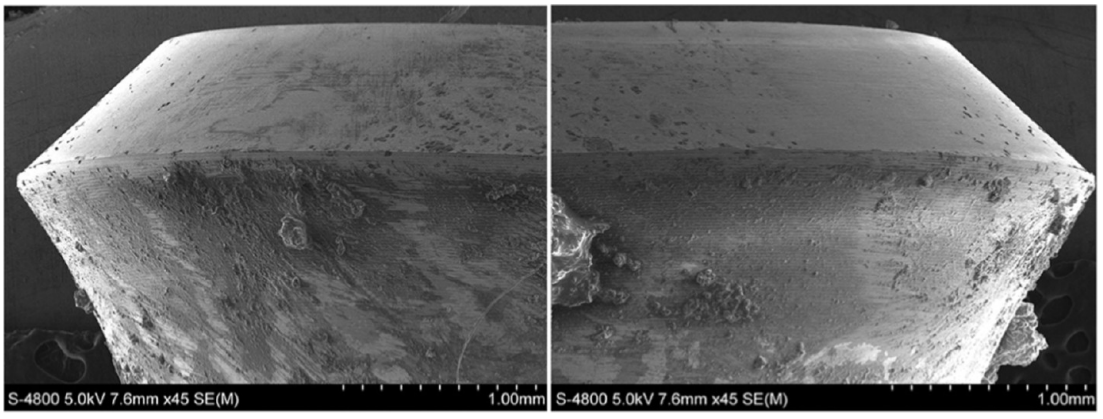

Figure 10. SEM images of the neck of the implant after the dynamic fatigue test, showing that the neck of the implant was intact and undamaged.

compatibility between the implant and abutment. This process offers a valuable reference for the manufacturing of AM titanium implants.

Dental implants require suitable mechanical strength, biocompatibility, and the capability to promote or, at a minimum, not impede bone regeneration and osseointegration.[19] AM titanium alloy implants exhibit high strength but limited elongation, restricting their broader clinical applications.[20] During the forming process, the rapid cooling rate of AM technology leads to the formation of a significant amount of acicular α' martensite within the crystals of AM titanium alloy. The primary advantages of this structure are its high strength and hardness, although it lacks sufficient ductility.[21] This is the main reason why SLM titanium alloys usually undergo subsequent heat treatment processes after forming, especially for dental implants that need to carry complex chewing forces in the mouth, and their ductility has relatively strict requirements.[22] The tensile property data obtained in this study are comparable to those reported in other literature. Vrancken et al.[23] screened a series of heat treatment regimens and found that the yield strength and tensile strength of SLM titanium alloy are 955 ± 6 MPa and 1004 ± 6 MPa, respectively, under the furnace cooling process at 850 °C for 2 h. The elongation rate also increased to 12.84 ± 1.36%. Liang et al.[24] carried out heat treatment at 800 and 850 °C for 4 h, followed by air cooling. The SLM titanium alloy sample

https://doi.org/10.1021/acsomega.4c09131
ACS Omega 2024, 9, 51591−51603

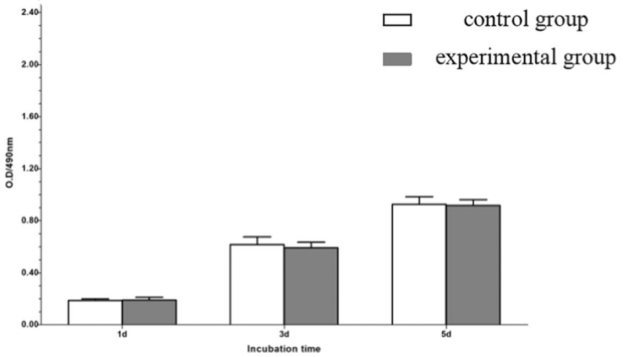

Figure 11. OD value of the MTT assay showing the cell proliferation of MG-63 cells of the experimental group and control group (n = 3). Data are presented as mean ± SD.

contained the most β and the smallest lamellar structure, which made it have good plasticity (12.2%−12.4%) and ultimate tensile strength (1033−1069 MPa). Generally, when used under no special stress conditions, SLM titanium alloy only needs to be destressed and annealed, and the temperature selection does not exceed 800 °C. In order to make a favorable change in the structure and significantly improve the comprehensive mechanical properties of SLM titanium alloy, the heat treatment temperature should reach more than 800 °C.[25,26] Therefore, the heat treatment system adopted in this study is as follows: state: annealing; temperature: 820 °C; holding time: 1.5 h; as the furnace cools, this is also the system recommended by the GB/T39247-2020 heat treatment process specification for AM metal parts. The results showed that heat treatment improved the plasticity of the 3D-printed titanium implants. Figure 9A shows that the fracture of the formed tensile specimen has almost no shrinkage, indicating that sudden fracture has occurred. Further observation of the frontal morphology of the section under electron microscopy (Figure 9B,C) shows that the fracture surface mainly presents two morphologies: one is a small step with a flat surface; the second is a shallow dimple. From the small step with a relatively flat surface, it can be seen that the crack propagation is transgranular, which is a typical transgranular brittle fracture, which is consistent with the characteristics of the SLM process forming a brittle and hard martensitic structure. Figure 9 also shows the appearance of a fracture of the tensile specimen after heat treatment. Viewed from the side, the fracture of the heat-treated specimen can be seen to shrink obviously. The microscopic morphology of the front section was observed by electron microscopy. It was found that large and deep dimpling appeared on the fracture surface, which is a typical ductile fracture feature and a manifestation of plastic enhancement. Corresponding to the results of the tensile test, it is conducive to the complex stress conditions of the implant during mastication. Table 1 shows the tensile performance results, confirming that the annealed form of 3D-printed titanium implants can meet the standards for the clinical application of titanium alloy forgings.

Biocompatibility of implant materials is essential for its application in the human body.[27] Some scholars have posited that the metal AM process could alter the composition of metal elements or impact other material properties, potentially affecting the biocompatibility of the fabricated parts.[28] In this study, extract test results indicated no significant difference in OD values between the experimental and blank control groups ($P > 0.05$), classifying cytotoxicity as grade 0. Indeed, not all printing technologies result in changes to alloy composition; for instance, SLM technology is conducted in an inert gas environment, avoiding processes that could alter metal element composition.[29] Xie et al.[30] confirmed that partially melted Ti_6Al_4 V particles on the surface of SLM porous titanium disks increased bacterial adhesion, potentially elevating the risk of implant infection. Furthermore, these partially melted particles inhibited the osteogenic activity of the hBMSCs. Consequently, sandblasting and acid etching were employed to remove loosely bound powder particles from the implant's surface, mitigating their impact on cellular biological functions.[31]

After the implant is implanted into the jaw, the initial stability is obtained through mechanical contact with the bone, and then the metabolic activity of bone formation begins. Bone marrow mesenchymal stem cells adhere, proliferate, and differentiate on the implant surface and finally form bone matrix, which is very important for the formation of osseointegration. Alizarin red can combine with calcium ions to form a fuchsia or red complex, which is a commonly used experimental method to evaluate osteogenic mineralization. Through Alizarin red staining experiment, DUAN et al.[32] observed that denser mineralized nodules were found on the titanium surface of SLM than on the surface of SLA. The results showed that after 14 days of osteogenic induction, there was no significant difference in the size and density of mineralized nodules between the experimental group and the control group (Figure 12). It is proven that the surface of SLM titanium is also beneficial to promote osteogenic mineralization, which provides an experimental basis for the effective promotion of bone union with SLM titanium implants.

In this study, the mandible of the implant beagle was sectioned, and the quantitative analysis of histomorphology showed that there was a gradual increase of new bone

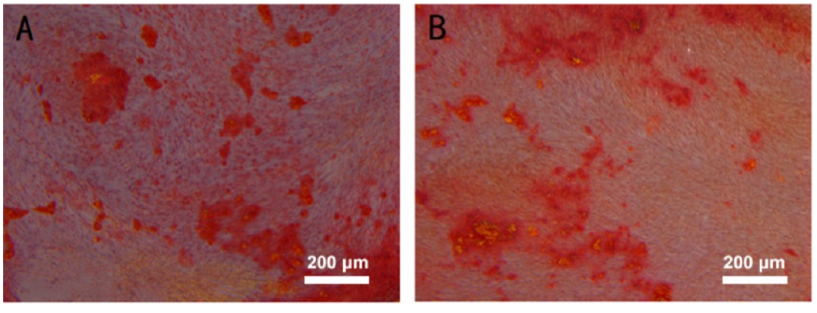

Figure 12. Alizarin red staining was used to detect the extracellular matrix mineralization of BMSCs (A: experimental group; B: control group).

https://doi.org/10.1021/acsomega.4c09131
ACS Omega 2024, 9, 51591−51603

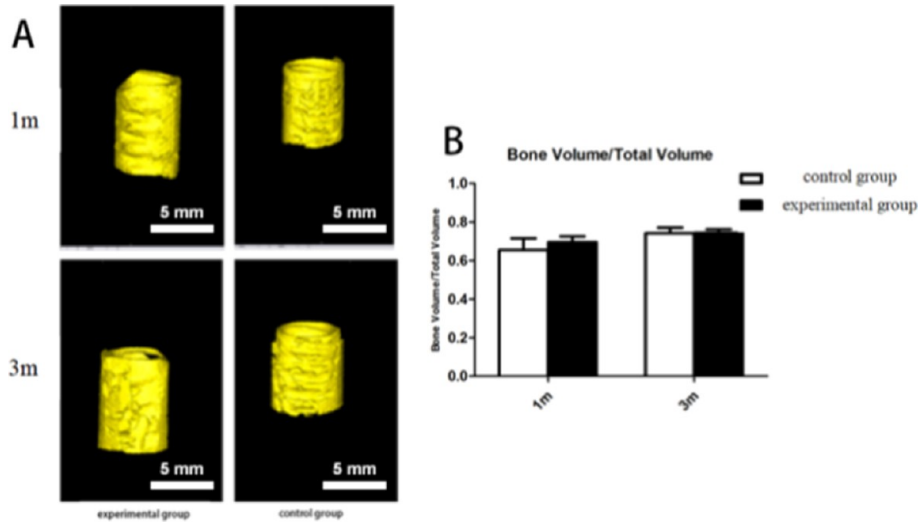

Figure 13. Results of micro-CT at 1 month and 3 months postimplantation. (A) Three-dimensional reconstruction map. (B) Bone volume fraction (n = 3). Data are presented as mean ± SD.

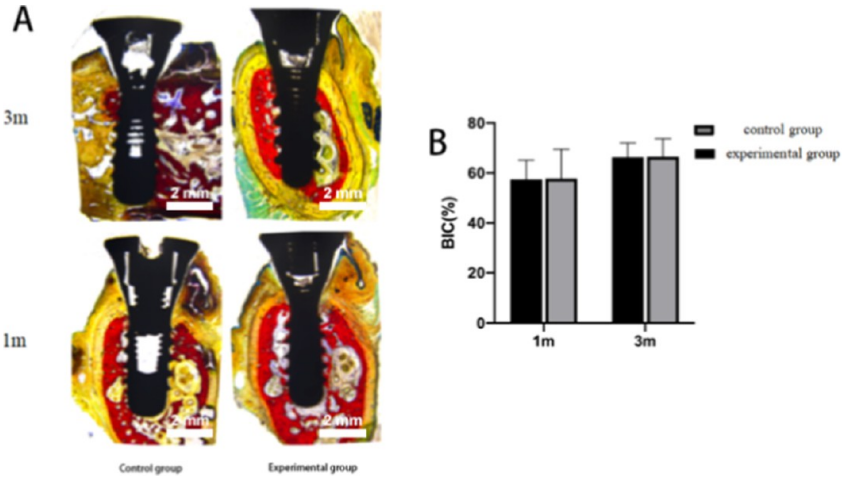

Figure 14. Evaluation of osseointegration for each group of implants at 1 month and 3 months postimplantation. (A) Hard tissue section (VG staining). (B) Comparison of BIC % between two groups (n = 3). Data are presented as mean ± SD.

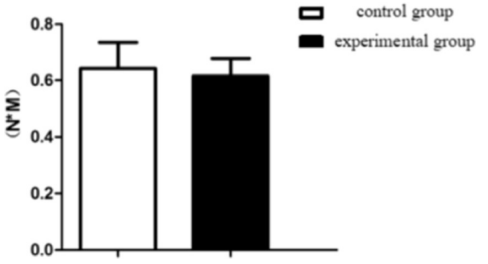

Figure 15. After 3 months of implantation, fresh bone blocks from the implant area were extracted for a torque-out test to measure the removal torque values of each group of implants (n = 5). Data are presented as mean ± SD.

formation around the implant in both groups at 1 or 3 months after healing and there was no significant difference in BIC between the two groups at the two time points. The results of this study are similar to those of Duan et al.[32] who compared the osseointegration effects of SLM titanium alloy implants and sandblasted acid-etched surface implants in type 2 diabetic rats. Histological results showed that there was no significant difference in BIC % between the two groups after 8 weeks of healing. In human studies, Mangano et al.[33] evaluated the histology of two three-dimensional-printed titanium implants that were broken after 5 years of functional load and found that the mature lamellar bone was in close contact with the surface of three-dimensional-printed titanium implants, with an average BIC % of 66.1 ± 4.5%, similar to the results obtained in this study. During implant implantation, the rough surface of the implant has a certain mechanical friction, which helps it obtain higher initial stability. In addition, a certain range of surface roughness also promotes the biological function of osteoblast adhesion, proliferation, and differentiation. The three-dimensional-printed titanium implant has a rough surface. The surface roughness can be further controlled in a better range by reasonably controlling the process parameters and subsequent supplementary surface treatment because some studies have shown that osteoblasts are most active when the average Ra value of the implant surface is 3−5 μm. The surface of the SLM titanium alloy was polished by laser. The Ra value of the polished sample decreased to 2.1 μm. The surface contact angle decreased to 68.5° ± 2°. The adhesion and proliferation of MC3T3-E1 cells on the polished sample

https://doi.org/10.1021/acsomega.4c09131
ACS Omega 2024, 9, 51591−51603

were significantly higher than those of the unpolished sample.[3] In this study, the surface roughness of the inner bone segment of the implant was not measured, but from the electron microscope image of the surface morphology of the implant after sandblasting and acid etching (Figure 6), the loosely bound powder particles on the implant surface decreased obviously, and the surface morphology is similar to that of the traditional sandblasted acid-etched implant; that is, a large pit-like surface is formed after sandblasting, which becomes small and irregular after acid etching. This may be one of the reasons why the bone volume fraction and bone binding rate of the two groups of implants are basically the same. In addition to the inherent surface roughness, there was a surface pore structure with a pore diameter of about 300 μm on the surface of the three-dimensional-printed titanium implant in the experimental group.

Porous surfaces are an important structural feature to promote bone regeneration. It not only increases the implant−bone contact area but also provides space for blood vessels and new bone to grow inward.[4−6] Unlike solid surface implants, bone tissue can only be attached to the surface and cannot grow in.[7] Pore diameter and porosity are the key geometric parameters in the design of a porous structure, and the ideal pore diameter and porosity directly affect the osteogenic effect of porous implants.[8,9] In the design process of using 3D-printing technology, different pore sizes and porosities can be adjusted to induce osteogenesis. It is generally believed that the minimum pore diameter allowed for cell growth is 100 μm, but in order to reduce the impact on mechanical properties, the maximum pore diameter is limited to 1000 μm, and the research on pore size is mostly focused on this range.[10,11] Huang et al.[34] designed two kinds of porous implants. Type I uses a circular porous scaffold structure with a pore size range of 50−200 μm, and type II uses bone trabecular tissue similar to cancellous bone with a pore size range of 300−500 μm with a porosity of 36% and 55%, respectively. The results of the pullout test showed that the maximum pullout strength of the two implants after 12 week healing period was 413.1 N and 493.2 N, respectively, which was higher than that of the solid surface implant, which confirmed that the bone growth in the pore structure could significantly increase the osseointegration strength. Wally et al.[35] observed that different pore sizes had no effect on cell viability. In the in vitro experiment, it was found that the maximum calcium deposition appeared in the 400 μm pore diameter sample. Taniguchi et al.[36] used SLM to prepare three kinds of titanium implants (300, 600, and 900 μm, respectively). In vivo experiments revealed that 600 μm implants had the strongest adhesion to bone tissue. Hara et al.[37] observed that the titanium implants with diameters of 500, 640, and 800 μm had similar bone growth. After a healing period of 4 to 12 weeks, the bone area of the three kinds of pore diameter samples increased by 40%−60%, while the bone area of 1000 μm pore diameter samples did not increase during this period of time. Bone growth is less. In short, there is no consensus on the most suitable parameters for osteogenesis induction. However, according to the above research results, the pore size range of 200−600 μm seems to be more favorable for cell growth in vitro and osteogenesis in vivo. Therefore, in this study, the pore diameter of the implant was set to 300 μm. We used SolidWorks software to build a 3D model of the implant. We designed the porous structure of the implant surface: 150 μm thick, 300 μm aperture, 100 μm edge diameter, diamond structure (Figure 6).

Density is one of the most important indexes to measure the quality of parts manufactured by SLM. It determines whether the parts can be used in practice and affects the mechanical properties and physical and chemical properties of the parts. There are many factors that affect the density of parts made by increasing the number of materials. In addition to equipment, materials, and man-made and environmental factors, the most important factors are laser power, scanning speed, scanning distance, powder layer thickness, and scanning strategy.[19] The SLM technology used in this study is based on the full melting mechanism, which has high density and few internal defects.[20] The density of SLM implants is measured by the Archimedes drainage method. The results show that the average density of the three samples is 4.08 g/cm^3.

Bone volume to total volume (BV/TV) directly reflects changes in bone mass and serves as a primary parameter for evaluating osseointegration of implants.[15] In this study, BV/TV ratios for both implant groups exhibited an upward trend throughout the healing period, signifying a gradual increase in new bone formation on the implant surfaces. Quantitative micro-CT analysis revealed no significant differences in BV/TV between the experimental and control groups at 1 and 3 months, suggesting that implants in the experimental group possessed an osseointegration capability comparable to that of traditional SLA surface implants.

Tissue sections' primary advantage lies in providing tissue response information, serving as robust evidence for evaluating implant osseointegration.[38] Therefore, following micro-CT imaging, bone growth around the implant was further assessed using nondecalcified tissue sections. Histomorphological quantitative analysis revealed a gradual increase in new bone formation around the implant in both groups, with no significant differences in BIC observed at either 1 or 3 months posthealing. Mangano et al.[33] assessed the histology of two three-dimensional-printed titanium implants that fractured after five years under functional load. They discovered mature lamellar bone in close contact with the surface of the three-dimensional-printed titanium implants, reporting an average BIC of 66.1 ± 4.5%, paralleling the findings of this study. The rough surface of the implant during implantation provides mechanical friction, aiding in achieving a higher initial stability. Moreover, a specific range of surface roughness enhances osteoblast adhesion, proliferation, and differentiation.[29,39] AM titanium implants possess a naturally rough surface. Figure 8 illustrates that loosely bound powder particles on the implant surface are significantly reduced, rendering the surface morphology akin to that of traditional SLA implants. This similarity may account for the comparable bone volume fraction and bone contact rates observed between the two groups of implants.

Removal torque is directly proportional to the contact area between the implant and the bone tissue. Consequently, removal torque testing is frequently employed to assess the strength of osseointegration.[40] The results showed that after 3 months of implant healing, the removal torque of the control group was slightly higher than that of the experimental group, but there was no significant difference between the two groups.

5. CONCLUSIONS

In this study, 3D printing was employed to fabricate the implant structure, followed by mechanical processing to refine the abutment connection and the neck. Mechanical property tests indicated that heat-treated, 3D-printed titanium alloy

https://doi.org/10.1021/acsomega.4c09131
ACS Omega 2024, 9, 51591−51603

dental implants exhibit significant tensile strength and fatigue resistance, making them capable of withstanding robust chewing forces in the oral cavity. In vitro findings revealed that the sandblasted and acid-etched 3D-printed titanium alloy exhibited negligible cytotoxicity, with osteoblast differentiation of hMSCs being more pronounced compared to the control group. In vivo studies showed no significant differences in bone volume fraction, BIC rate, and unscrewing torque between the 3D-printed titanium alloy dental implants and commercial SLA surface implants at both 1 and 3 months postimplantation. Our results demonstrated that combining 3D printing with subsequent machining is an effective method for manufacturing two-stage titanium dental implants. These two-stage titanium implants, which integrate both manufacturing techniques, exhibit satisfactory molding precision, mechanical properties, biocompatibility, and osseointegration performance. This approach provides a valuable reference for the development of 3D-printed two-stage titanium implants.

AUTHOR INFORMATION

Corresponding Author

Dehua Li − *State Key Laboratory of Oral & Maxillofacial Reconstruction and Regeneration & National Clinical Research Center for Oral Diseases & Shaanxi Engineering Research Center for Dental Materials and Advanced Manufacture, Department of Oral Implants, School of Stomatology, The Fourth Military Medical University, Xi'an 710032 Shaanxi, P. R. China*; Email: lidehua@fmmu.edu.cn

Authors

Hongbo Wei − *State Key Laboratory of Oral & Maxillofacial Reconstruction and Regeneration & National Clinical Research Center for Oral Diseases & Shaanxi Engineering Research Center for Dental Materials and Advanced Manufacture, Department of Oral Implants, School of Stomatology, The Fourth Military Medical University, Xi'an 710032 Shaanxi, P. R. China*; orcid.org/0000-0001-5167-031X

Shitou Huang − *State Key Laboratory of Oral & Maxillofacial Reconstruction and Regeneration & National Clinical Research Center for Oral Diseases & Shaanxi Engineering Research Center for Dental Materials and Advanced Manufacture, Department of Oral Implants, School of Stomatology, The Fourth Military Medical University, Xi'an 710032 Shaanxi, P. R. China*

Yi Liu − *State Key Laboratory of Oral & Maxillofacial Reconstruction and Regeneration & National Clinical Research Center for Oral Diseases & Shaanxi Engineering Research Center for Dental Materials and Advanced Manufacture, Department of Oral Implants, School of Stomatology, The Fourth Military Medical University, Xi'an 710032 Shaanxi, P. R. China*

Complete contact information is available at: https://pubs.acs.org/10.1021/acsomega.4c09131

Author Contributions

†Hongbo Wei and Shitou Huang contributed equally to this work. **Hongbo Wei:** writing—review and editing, writing—original draft, visualization, validation, supervision, software, resources, project administration, methodology, investigation, funding acquisition, formal analysis, data curation, and conceptualization. **Shitou Huang:** writing—review and editing, writing—original draft, visualization, validation, software, resources, methodology, investigation, formal analysis, data curation, and conceptualization. **Yi Liu:** writing—review and editing, data curation, and conceptualization. **Dehua Li:** writing—review and editing, visualization, validation, supervision, resources, methodology, investigation, conceptualization, and project administration.

Funding

This study was supported by the Key Research and Development Plan of Shaanxi Province (2022SF-165).

Notes

The authors declare no competing financial interest.

REFERENCES

(1) Oliveira, T. T.; Reis, A. C. Fabrication of dental implants by the additive manufacturing method: a systematic review. *J. Prosthet. Dent.* **2019**, *122*, 270−274.

(2) Gaviria, L.; Salcido, J. P.; Guda, T.; Ong, J. L. Current trends in dental implants. *J. Korean Assoc. Oral Maxillofac. Surg.* **2014**, *40*, 50.

(3) Huang, S.; Wei, H.; Li, D. Additive manufacturing technologies in the oral implant clinic: a review of current applications and progress. *Front. Bioeng. Biotechnol.* **2023**, *11*, 1100155.

(4) Pałka, K.; Pokrowiecki, R. Porous titanium implants: a review. *Adv. Eng. Mater.* **2018**, *20*, 1700648.

(5) Revilla León, M.; Sadeghpour, M.; Özcan, M. A review of the applications of additive manufacturing technologies used to fabricate metals in implant dentistry. *J. Prosthodontics* **2020**, *29*, 579−593.

(6) Attarilar, S.; Ebrahimi, M.; Djavanroodi, F.; Fu, Y.; Wang, L.; Yang, J. 3d printing technologies in metallic implants: a thematic review on the techniques and procedures. *Int. J. Bioprint.* **2021**, *7*, 306.

(7) Liu, M.; Wang, Y.; Zhang, S.; Wei, Q.; Li, X. Success factors of additive manufactured root analogue implants. *ACS Biomater. Sci. Eng.* **2022**, *8*, 360−378.

(8) Dantas, T.; Madeira, S.; Gasik, M.; Vaz, P.; Silva, F. Customized root-analogue implants: a review on outcomes from clinical trials and case reports. *Materials* **2021**, *14*, 2296.

(9) Saeidi Pour, R.; Freitas Rafael, C.; Engler, M. L. P. D.; Edelhoff, D.; Klaus, G.; Prandtner, O.; Berthold, M.; Liebermann, A. Historical development of root analogue implants: a review of published papers. *Br. J. Oral Maxillofac. Surg.* **2019**, *57*, 496−504.

(10) Estévez-Pérez, D.; Bustamante-Hernández, N.; Labaig-Rueda, C.; Solá-Ruíz, M. F.; Amengual-Lorenzo, J.; García-Sala Bonmatí, F.; Zubizarreta-Macho, A.; Agustín-Panadero, R. Comparative analysis of peri-implant bone loss in extra-short, short, and conventional implants. A 3-year retrospective study. *Int. J. Environ. Res. Public Health* **2020**, *17*, 9278.

(11) Liu, Y.; Sing, S. L.; Lim, R.; Yeong, W. Y.; Goh, B. T. Preliminary investigation on the geometric accuracy of 3d printed dental implant using a monkey maxilla incisor model. *Int. J. Bioprint.* **2022**, *8*, 476.

(12) Chen, J.; Zhang, Z.; Chen, X.; Zhang, C.; Zhang, G.; Xu, Z. Design and manufacture of customized dental implants by using reverse engineering and selective laser melting technology. *J. Prosthet. Dent.* **2014**, *112*, 1088−1095.

(13) de Oliveira Campos, F.; Araujo, A. C.; Jardini Munhoz, A. L.; Kapoor, S. G. The influence of additive manufacturing on the micromilling machinability of ti6al4v: a comparison of slm and commercial workpieces. *J. Manufact. Process.* **2020**, *60*, 299−307.

(14) Nan Kuo, C.; Wang, Y. P.; Chua, C. K. Effect of electropolishing on mechanical property enhancement of ti6al4v porous materials fabricated by selective laser melting. *Virtual Phys. Prototyp.* **2022**, *17*, 919−931.

(15) Zhang, J.; Liu, J.; Wang, C.; Chen, F.; Wang, X.; Lin, K. A comparative study of the osteogenic performance between the hierarchical micro/submicro-textured 3d-printed ti6al4v surface and the sla surface. *Bioact. Mater.* **2020**, *5*, 9−16.

(16) Srinivasan, D.; Singh, A.; Reddy, A. S.; Chatterjee, K. Microstructural study and mechanical characterisation of heat-treated direct metal laser sintered ti6al4v for biomedical applications. *Mater. Technol.* **2022**, *37*, 260−271.
(17) Bartolomeu, F.; Gasik, M.; Silva, F. S.; Miranda, G. Mechanical properties of ti6al4v fabricated by laser powder bed fusion: a review focused on the processing and microstructural parameters influence on the final properties. *Metals* **2022**, *12*, 986.
(18) Du, W.; Bai, Q.; Zhang, B. A novel method for additive/subtractive hybrid manufacturing of metallic parts. *Procedia Manuf.* **2016**, *5*, 1018−1030.
(19) van Oirschot, B. A. J. A.; Zhang, Y.; Alghamdi, H. S.; Cordeiro, J. M.; Nagay, B. E.; Barao, V. A. R.; de Avila, E. D.; van den Beucken, J. J. J. P. Surface engineering for dental implantology: favoring tissue responses along the implant. *Tissue Eng., Part A* **2022**, *28*, 555−572.
(20) Liu, S.; Shin, Y. C. Additive manufacturing of ti6al4v alloy: a review. *Mater. Des.* **2019**, *164*, 107552.
(21) DebRoy, T.; Wei, H. L.; Zuback, J. S.; Mukherjee, T.; Elmer, J. W.; Milewski, J. O.; Beese, A. M.; Wilson-Heid, A.; De, A.; Zhang, W. Additive manufacturing of metallic components − process, structure and properties. *Prog. Mater. Sci.* **2018**, *92*, 112−224.
(22) Ter Haar, G.; Becker, T. Selective laser melting produced ti-6al-4v: post-process heat treatments to achieve superior tensile properties. *Materials* **2018**, *11*, 146.
(23) Vrancken, B.; Thijs, L.; Kruth, J.; Van Humbeeck, J. Heat treatment of ti6al4v produced by selective laser melting: microstructure and mechanical properties. *J. Alloy. Compd.* **2012**, *541*, 177−185.
(24) Liang, Z.; Sun, Z.; Zhang, W.; Wu, S.; Chang, H. The effect of heat treatment on microstructure evolution and tensile properties of selective laser melted ti6al4v alloy. *J. Alloy. Compd.* **2019**, *782*, 1041−1048.
(25) Su, C.; Yu, H.; Wang, Z.; Yang, J.; Zeng, X. Controlling the tensile and fatigue properties of selective laser melted ti−6al−4v alloy by post treatment. *J. Alloy. Compd.* **2021**, *857*, 157552.
(26) Gehrke, S. A.; Pérez-Díaz, L.; Dedavid, B. A. Quasi-static strength and fractography analysis of two dental implants manufactured by direct metal laser sintering. *Clin. Implant Dent. R.* **2018**, *20*, 368−374.
(27) Wysocki, B.; Maj, P.; Sitek, R.; Buhagiar, J.; Kurzydłowski, K.; Święszkowski, W. Laser and electron beam additive manufacturing methods of fabricating titanium bone implants. *Appl. Sci.* **2017**, *7*, 657.
(28) Ilea, A.; Timuş, D.; Petrescu, N. B.; Soriţău, O.; Boşca, B. A.; Mager, V.; Barbu-Tudoran, L.; Băbţan, A. M.; Câmpian, R. S.; Barabás, R. An in vitro study on the biocompatibility of titanium implants made by selective laser melting. *Biotechnol. Bioprocess.* **2019**, *24*, 782−792.
(29) Mangano, C.; Piattelli, A.; Scarano, A.; Raspanti, M.; Shibli, J. A.; Mangano, F. G.; Perrotti, V.; Iezzi, G. A light and scanning electron microscopy study of human direct laser metal forming dental implants. *Int. J. Periodontics Restorative Dent.* **2014**, *34*, e9−e17.
(30) Xie, K.; Guo, Y.; Zhao, S.; Wang, L.; Wu, J.; Tan, J.; Yang, Y.; Wu, W.; Jiang, W.; Hao, Y. Partially melted ti6al4v particles increase bacterial adhesion and inhibit osteogenic activity on 3d-printed implants: an in vitro study. *Clin. Orthop. Relat. Res.* **2019**, *477*, 2772−2782.
(31) Vaithilingam, J.; Prina, E.; Goodridge, R. D.; Hague, R. J. M.; Edmondson, S.; Rose, F. R. A. J.; Christie, S. D. R. Surface chemistry of ti6al4v components fabricated using selective laser melting for biomedical applications. *Mater. Sci. Eng. Carbon* **2016**, *67*, 294−303.
(32) Duan, Y.; Liu, X.; Zhang, S.; Wang, L.; Ding, F.; Song, S.; Chen, X.; Deng, B.; Song, Y. Selective laser melted titanium implants play a positive role in early osseointegration in type 2 diabetes mellitus rats. *Dent. Mater. J.* **2020**, *39*, 214−221.
(33) Mangano, F.; Mangano, C.; Piattelli, A.; Iezzi, G. Histological evidence of the osseointegration of fractured direct metal laser sintering implants retrieved after 5 years of function. *Biomed. Res. Int.* **2017**, *2017*, 1−7.
(34) Huang, C.; Li, M.; Tsai, P.; Kung, P.; Chen, S.; Sun, J.; Tsou, N. Novel design of additive manufactured hollow porous implants. *Dent. Mater.* **2020**, *36*, 1437−1451.
(35) Wally, Z. J.; Haque, A. M.; Feteira, A.; Claeyssens, F.; Goodall, R.; Reilly, G. C. Selective laser melting processed ti6al4v lattices with graded porosities for dental applications. *J. Mech. Behav. Biomed.* **2019**, *90*, 20−29.
(36) Taniguchi, N.; Fujibayashi, S.; Takemoto, M.; Sasaki, K.; Otsuki, B.; Nakamura, T.; Matsushita, T.; Kokubo, T.; Matsuda, S. Effect of pore size on bone ingrowth into porous titanium implants fabricated by additive manufacturing: an in vivo experiment. *Mater. Sci. Eng. Carbon* **2016**, *59*, 690−701.
(37) Hara, D.; Nakashima, Y.; Sato, T.; Hirata, M.; Kanazawa, M.; Kohno, Y.; Yoshimoto, K.; Yoshihara, Y.; Nakamura, A.; Nakao, Y.; Iwamoto, Y. Bone bonding strength of diamond-structured porous titanium-alloy implants manufactured using the electron beam-melting technique. *Mater. Sci. Eng. Carbon* **2016**, *59*, 1047−1052.
(38) Hyzy, S. L.; Cheng, A.; Cohen, D. J.; Yatzkaier, G.; Whitehead, A. J.; Clohessy, R. M.; Gittens, R. A.; Boyan, B. D.; Schwartz, Z. Novel hydrophilic nanostructured microtexture on direct metal laser sintered ti-6al-4v surfaces enhances osteoblast response in vitro and osseointegration in a rabbit model. *J. Biomed. Mater. Res., Part A* **2016**, *104*, 2086−2098.
(39) Chen, J.; Xiao, Z.; Yangpeng, S.; Deng, F.; Zhiguang, Z. Production of inter-connective porous dental implants by computer-aided design and metal three-dimensional printing. *J. Biomater. Appl.* **2020**, *34*, 1227−1238.
(40) Shah, F. A.; Snis, A.; Matic, A.; Thomsen, P.; Palmquist, A. 3d printed ti6al4v implant surface promotes bone maturation and retains a higher density of less aged osteocytes at the bone-implant interface. *Acta Biomater.* **2016**, *30*, 357−367.

https://doi.org/10.1021/acsomega.4c09131
ACS Omega 2024, 9, 51591−51603